Geophysical and Astrophysical Fluid Dynamics
Vol. 00, No. 00, 00 Month 20xx, 1–17

Instabilities in a Staircase Stratified Shear Flow

G. Ponetti†*, N. J. Balmforth‡ and T. S. Eaves‡
†Department of Mathematics, University of Palermo, Via Archirafi 34, 90123, Palermo, PA, Italy
‡Department of Mathematics, University of British Columbia, 1984 Mathematics Rd.,
Vancouver, BC, V6T 1Z2, Canada

(*Received 00 Month 20xx; final version received 00 Month 20xx*)

We study stratified shear flow instability where the density profile takes the form of a staircase of interfaces separating uniform layers. Internal gravity waves riding on density interfaces can resonantly interact due to a background shear flow, resulting in the Taylor-Caulfield instability. The many steps of the density profile permit a multitude of interactions between different interfaces, and a rich variety of Taylor-Caulfield instabilities. We analyse the linear instability of a staircase with piecewise-constant density profile embedded in a background linear shear flow, locating all the unstable modes and identifying the strongest. The interaction between nearest-neighbour interfaces leads to the most unstable modes. The nonlinear dynamics of the instabilities are explored in the long-wavelength, weakly stratified limit (the defect approximation). Unstable modes on adjacent interfaces saturate by rolling up the intervening layer into a distinctive billow. These nonlinear structures coexist when stacked vertically and are bordered by the sharp density gradients that are the remnants of the steps of the original staircase. Horizontal averages remain layer-like.

Keywords: Stratified shear flow instability, layers

1. Introduction

In some areas of the world's oceans, the stratification of temperature and salt takes the form of long-lived "staircases" (Schmitt 1994, Carpenter and Timmermans 2012) of sharp steps buffering homogeneous layers. These structures owe their existence to small-scale fluid mechanical processes deriving from the difference in the rates at which heat and salt diffuse, but can become so large that they occupy a good fraction of the water column and extend in the horizontal by many kilometers. Similar staircases have been observed in lakes and solar ponds, and suggested to occur inside stars and magma chambers (Turner 1985). Layering can also occur in quite different settings and without any double diffusion, such as when a stably stratified fluid is vigorously mixed by turbulence (Park *et al.* 1994, Balmforth *et al.* 1998) or subject to horizontally sheared and directed flow (Oglethorpe *et al.* 2013).

If a stratified fluid flows horizontally with vertical shear, a number of linear instabilities can appear, the most familiar of which is the celebrated Kelvin-Helmholtz instability (Drazin and Reid 2004), which can occasionally be seen to pattern clouds in our own atmosphere as well as those of the giant planets. This instability is sometimes interpreted in terms of the interaction of waves riding on sharp interfaces of vorticity (Cairns 1979, Baines and Mitsudera 1994, Carpenter *et al.* 2011). In fact, when there are also interfaces in the background density stratification, a number of other, less well-known instabilities can appear. Of these, the Holmboe instability has received more attention, and is interpreted to arise through the interaction of a wave supported by a vorticity interface interacting with a gravity wave riding

*Corresponding author. Email: giordanoponetti@gmail.com

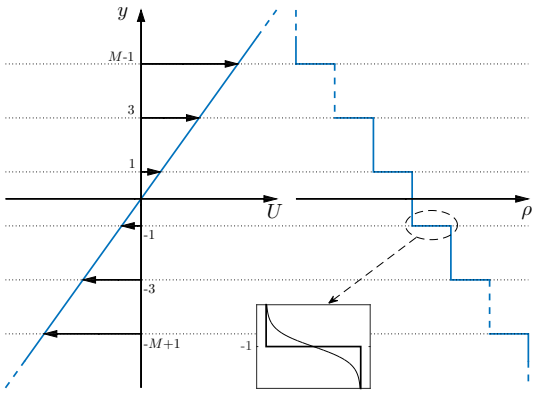

Figure 1. A sketch of the equilibrium linear shear flow and stepped density profile for a staircase with M fluid interfaces (with $M = 6$). In the example shown, the density interfaces are equally spaced and of equal strength. The inset shows the structure of the two interface profiles that we consider: a discontinuous interface (thick line) and a hyperbolic tangent interface (thin curve).

on a density interface (Alexakis 2005, Carpenter *et al.* 2010, 2011). A third instability, pointed out by Taylor over eighty years ago, arises when two gravity waves riding on different density interfaces become coupled through ambient shear flow. This third instability has received very little consideration until quite recently (Caulfield 1994, Balmforth *et al.* 2012, Eaves and Caulfield 2017).

The existence of layered, stratified fluids lead one to speculate whether the interaction of a staircase with large-scale shear flow could play a key role in controlling the evolution of that structure and even limit its extent. In fact, layers are observed to possess distinctive dynamics over longer timescales, including merging and vertical migration. This is often interpreted to result from a nonlinear interaction between adjacent layers and interfaces (Balmforth *et al.* 1998, Radko 2007). However, another possibility is that the staircase is evolving due to the excitation of a stratified shear instability. Indeed, the presence of a large number of density steps suggests that a wide array of instabilities of Taylor's type are feasible for a staircase.

This sets the stage for the current paper: we provide a linear stability analysis of a staircase in the presence of a vertical shear flow, mapping out the zoo of potential instabilities and determining the physical conditions required for their appearance. Continuing on to the nonlinear dynamics, we explore the subsequent evolution of a linear instability. An over-arching question is whether the instability destroys the staircase by rolling up each of the layers, or if nonlinear waves emerge that more gently disturb the structure, leaving it intact and potentially rationalizing the observed layer dynamics.

2. Formulation

2.1. *Governing equations*

We consider a two-dimensional, inviscid and non-diffusive, incompressible fluid under the effect of gravity g. Governing equations are given in the vorticity-buoyancy-streamfunction

formulation by

$$\hat{\zeta}_{\hat{t}} + \hat{\psi}_{\hat{x}}\hat{\zeta}_{\hat{y}} - \hat{\psi}_{\hat{y}}\hat{\zeta}_{\hat{x}} = \hat{b}_{\hat{x}}, \tag{1}$$

$$\hat{\zeta} = \hat{\psi}_{\hat{x}\hat{x}} + \hat{\psi}_{\hat{y}\hat{y}}, \tag{2}$$

$$\hat{b}_{\hat{t}} + \hat{\psi}_{\hat{x}}\hat{b}_{\hat{y}} - \hat{\psi}_{\hat{y}}\hat{b}_{\hat{x}} = 0 \tag{3}$$

where $\hat{b} = -g(\rho - \rho_0)/\rho_0$ is the buoyancy field, expressed in terms of the density ρ and a characteristic value ρ_0, $\hat{\zeta}$ is the vorticity and $\hat{\psi}$ is the streamfunction, defined so that the velocity field is $(\hat{u}, \hat{v}) = (-\hat{\psi}_{\hat{y}}, \hat{\psi}_{\hat{x}})$. Here, the hat decoration denotes dimensional quantities.

The domain is horizontally periodic and infinitely deep. The equilibrium velocity and density profiles are illustrated in figure 1. The velocity is a linear shear $(s\hat{y}, 0)$, where s is the shear rate. The density profile $\bar{\rho}$ consists of a group of stacked layers of constant density. The layer densities increase with depth in steps of $\Delta\rho_j$ over the j^{th} interface, which is centered at the level $\hat{y} = \hat{y}_j$. Altogether, there are M interfaces. In practice, we take M to be even and centre the staircase about $\hat{y} = 0$. The interfaces themselves are taken to be either discontinuous jumps, or continuous but relatively sharp with a smooth profile, as illustrated in figure 1.

We remove the dimensions from the system in (1)–(3) by scaling lengths by the typical layer thickness L, using $U = sL$ as a characteristic velocity, and L/U as the timescale:

$$(x, y) = L^{-1}(\hat{x}, \hat{y}), \quad t = L^{-1}U\hat{t}, \quad (u, v) = U^{-1}(\hat{u}, \hat{v}). \tag{4}$$

We further choose the unit U^2/L for the buoyancy and split the evolving perturbations from the background equilibrium by defining

$$\hat{\psi} = -\frac{1}{2}ULy^2 + UL\psi, \qquad \hat{\zeta} = \frac{U}{L} + \frac{U}{L}\zeta, \qquad \hat{b} = \frac{U^2}{L}B(y) + \frac{U^2}{L}b. \tag{5}$$

The dimensionless equations for the perturbations are then

$$\zeta_t + \psi_x\zeta_y - \psi_y\zeta_x + y\zeta_x = b_x \tag{6}$$

$$b_t + \psi_x b_y - \psi_y b_x + yb_x + G\psi_x = 0, \tag{7}$$

$$\zeta = \psi_{xx} + \psi_{yy}, \tag{8}$$

where the staircase profile is set by the buoyancy gradient,

$$G(y) \equiv B'(y) = \sum_{j=1}^{M} J_j\Theta(y - y_j), \qquad J_j = \frac{gL\Delta\rho_j}{\rho_0 U^2}, \tag{9}$$

with J_j the scaled density jump and we make one of the two selections,

$$\Theta(y) = \delta(y), \tag{10}$$

$$\Theta(y) = \frac{1}{2d}\mathrm{sech}^2(y/d), \tag{11}$$

to model a discontinuous or smooth interface, respectively; $\delta(y)$ is the delta-function, and for the latter, d is the characteristic interface thickness in units of L.

2.2. *The long wavelength, weakly stratified limit*

In the limit that the horizontal lengthscale is far larger than the vertical one and the stratification and mode amplitude remain relatively weak, the equations can be simplified using

asymptotic methods (Balmforth *et al.* 2012). This "stratified defect theory" begins with the introduction of a small parameter ε and the new variables,

$$\eta = \frac{y}{\varepsilon}, \quad \tau = \varepsilon t, \quad \Phi(x,\eta,\tau) = \varepsilon^{-2}\psi \quad \text{and} \quad \mathscr{Z}(x,\eta,\tau) = \varepsilon^{-1}(\zeta + b_y) \tag{12}$$

(together with a re-interpretation of L as a characteristic horizontal lengthscale). The asymptotic machinations then establish that the leading-order streamfunction is independent of the stretched vertical coordinate η, so that

$$\Phi \equiv \sum_{n=-\infty}^{\infty} \Phi_n(t) e^{inx}, \tag{13}$$

and we arrive at the Vlasov-like system,

$$\mathscr{Z}_\tau + \eta \mathscr{Z}_x + (\mathscr{Z}_\eta + \mathcal{G}_\eta)\Phi_x = 0 \qquad \text{and} \qquad \Phi_n = -\frac{1}{4\pi|n|}\int_0^{2\pi}\int_{-\infty}^{+\infty} e^{-inx}\,\mathscr{Z}\,\mathrm{d}\eta\mathrm{d}x, \tag{14}$$

with $\mathcal{G}(\eta) = \varepsilon^{-1}G(y)$.

3. Linear stability analysis

On linearizing (6)–(8), we may search for normal mode solutions with the form,

$$[\psi(x,y,t), \zeta(x,y,t), b(x,y,t)] = [\Psi(y), \mathcal{Z}(y), \mathcal{B}(y)]\, e^{ik(x-ct)}, \tag{15}$$

where k is the horizontal wavenumber and $c = c_r + ic_i$ is the complex phase velocity ($c_i > 0$ implying instability). We then recover the Taylor-Goldstein equation,

$$\left(\frac{d^2}{dy^2} - k^2\right)\Psi = -\frac{G\Psi}{(y-c)^2}. \tag{16}$$

We may turn (16) into an integral equation by using the Green's function of the operator on the right-hand side,

$$g(y,\xi) = -\frac{1}{2k}e^{-k|y-\xi|}. \tag{17}$$

Thence,

$$\Psi(y) = \frac{1}{2k}\int_{-\infty}^{+\infty} \frac{G(\xi)\Psi(\xi)}{(\xi-c)^2} e^{-k|y-\xi|}\mathrm{d}\xi. \tag{18}$$

In the defect limit, $\Psi(y) \sim$ *constant*, $(y,\xi) \to \varepsilon(\eta,\eta')$ and $G(y) \to \varepsilon\mathcal{G}(\eta)$, leading to the explicit dispersion relation (also following from (14); *cf.* Balmforth *et al.* (2012)),

$$2k = \int_{-\infty}^{+\infty} \frac{\mathcal{G}(\eta')\,\mathrm{d}\eta'}{(\eta'-c)^2}. \tag{19}$$

Ponetti (2017) provides a discussion of the linear stability of staircases in the defect approximation based on (19). Below, we explore the linear stability using the full problem (18).

3.1. *Sharp (discontinous) interfaces*

As argued in previous works (Sutherland 2010, Carpenter *et al.* 2011), TCI can be interpreted as a resonance between gravity waves supported by different density interfaces that arises when

the Doppler-shifting effect of the background flow allows their horizontal phase speeds to lock together. This resonance requires a suitable choice for the Richardson numbers J_j, which control the natural phase speed of the waves on the j^{th} interface. Indeed, one anticipates that a wave propagating to the right on that interface can be shifted by the background shear flow to resonate with the leftward travelling waves on the overlying $M-j$ interfaces. Thus, there are $\sum_{j=1}^{M}(M-j) = M^2 - \frac{1}{2}M(M+1) = \frac{1}{2}M(M-1)$ possible resonances altogether, occuring for different and suitably tuned values of the J_j.

3.1.1. *Unstable resonant modes*

For sharp (discontinuous) interfaces, $G = \sum_{j=1}^{M} J_j \delta(y-y_j)$, and the introduction of (9) and (10) into (18) immediately furnishes the polynomial matrix eigenvalue problem,

$$2k(y_j-c)^2 X_j = \sum_{l=1}^{M} J_l e^{-k|y_l-y_j|} X_l, \qquad X_j = \frac{\Psi(y_j)}{(y_j-c)^2}, \tag{20}$$

with $2M$ solutions for c.

The case $M=2$ and $J_1 = J_2 = J$ ($y_2 = -y_1 = 1$) was investigated by Taylor (1931) (see also Sutherland (2010)) and furnishes the explicit dispersion relation

$$c^4 - \left(\frac{J}{k}+2\right)c^2 + \frac{J^2}{4k^2}\left(1-e^{-4k}\right) - \left(\frac{J}{k}-1\right) = 0, \tag{21}$$

which predicts unstable modes with zero phase speed over a band on the $(k,J)-$plane between the two marginal stability curves,

$$J = J_{\pm}(k) = \frac{2k}{1 \pm e^{-2k}}. \tag{22}$$

A selection of results for more interfaces is shown in figure 2. The different rows of this figure show results for staircases with different choices for $J_j = J(1+\Delta_j)$ and $y_j = 2j - M - 1 + \delta_j$, where Δ_j and δ_j denote randomly chosen parameters that introduce asymmetries into the density profiles. The top row is for equally spaced steps of equal strength ($\Delta_j = \delta_j = 0$); the middle row has equal-strength steps that are located randomly ($\Delta_j = 0$, $\delta_j \neq 0$); in the lowest row the steps are equally spaced but have randomly chosen strengths ($\Delta_j \neq 0$, $\delta_j = 0$). The staircase profiles themselves are also plotted. In all the rows, the first two columns plot how c_r and c_i vary with J; the phase speed gradually changes as J increases, leading to mode crossings and resonances. The resonances create bands of finite width in J over which the resonant pair become unstable, leading to "bubbles" of positive c_i. For the case with equally spaced steps of equal strength, there is a large degree of degeneracy: multiple resonances occur at the same values of J, restricting the number of discernible instability bands. This degeneracy is lifted when the uniformity of the staircase is destroyed, and the full set of instability bands then becomes evident. The third column of figure 2 plots the instability bands on the $(k,J)-$plane. We conclude that, as expected, the multiplicity of steps in the density profile introduces a multitude of TCIs; a uniformity in the structure of the staircase merely leads to degenerate resonances and is not key to the appearance of unstable modes.

Figure 3 provides a closer look at the structure of the resonant instability bands for the staircase with steps of equal spacing and strength. We label the interfaces at $y = \pm 1$, ± 3 and ± 5 by $A^{\pm}$, $B^{\pm}$ and $C^{\pm}$, respectively. The figure identifies the resonances according to the interfaces providing the participating waves. The nearest neighbour interactions (A^+A^-, A^+B^+, A^-B^-, B^+C^+ and B^-C^-) have the strongest growth rates, with the interaction of the central steps (A^+A^-) with $c_r = 0$ being slightly more unstable. The interaction weakens

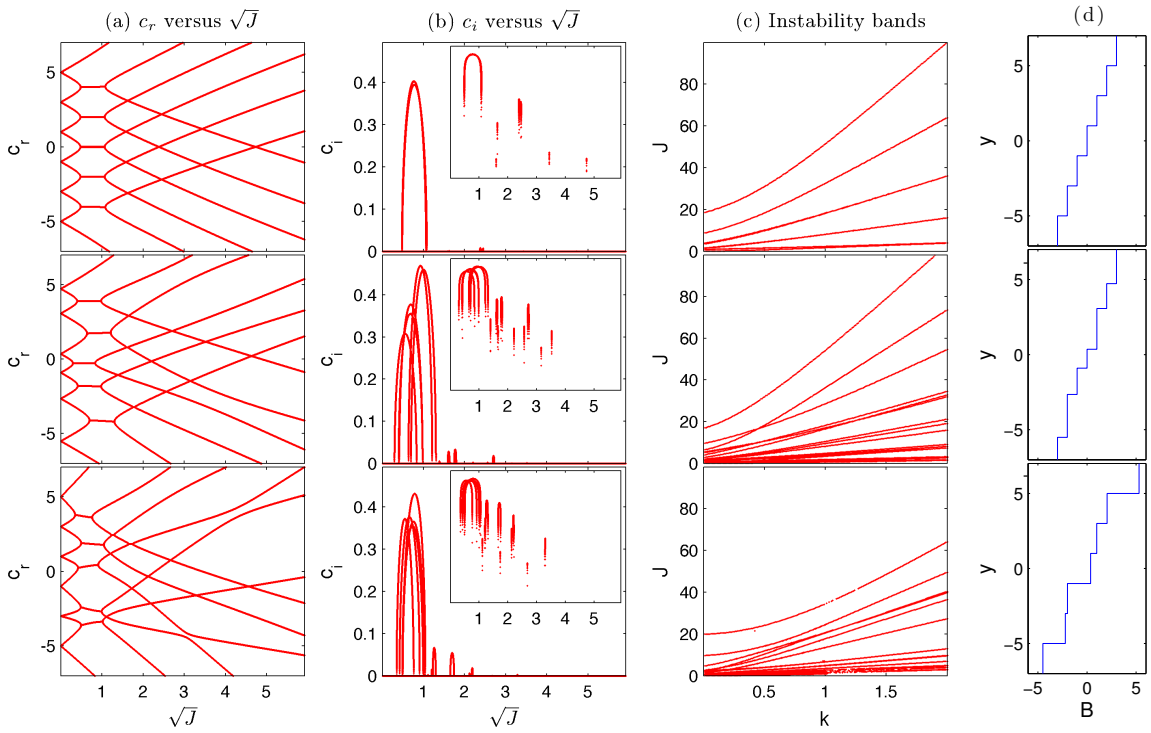

Figure 2. Eigenvalues and stability bands for staircases with $M = 6$ interfaces. The columns show (a) c_r and (b) c_i against $\sqrt{J}$ for $k = 0.2$, (c) the borders of the bands on the $(k, J)-$plane (the bands are too narrow to discern), and (d) the staircase profile $B(y)$. The inset in (b) shows $\log(|c_i|)$. The top row corresponds to equally spaced steps of equal strength. In the second row, the steps are located randomly, but have equal strength. In the bottom row, the steps are equally spaced, but have randomly chosen strengths.

as the distance between the interfaces increases, with C^+C^- providing the smallest growth rates and requiring the strongest stratification (J). Figure 4 shows how the growth rate of the "core" A^+A^- instability varies with the total number of interfaces M, and increases (but eventually saturates) with M.

One other interesting feature brought out in the final row of figure 2 is that the alignment of phase speed for different modes does not always prompt an unstable interaction: for $(\sqrt{J}, k) \approx (3.2, -4)$ and $(4.5, 4)$, two phase speeds approach one another but then avoid crossing. These modes correspond to waves that ride on different interfaces, but propagate naturally in the same direction (the phase speed of both waves either increases or decreases with $\sqrt{J}$); their phase speeds can become matched by the background shear when the interfaces have different strength. The interpretation of the avoidance of the resonant interaction is that these modes have the same sense of wave action (or pseudo-energy or pseudo-momentum) and cannot therefore couple together to form an unstable mode (Cairns 1979). When the modes propagate naturally in opposite directions (the slopes of c_r with $\sqrt{J}$ have different sign), they have opposite signs of wave action, allowing an unstable mode coupling.

3.1.2. *Instability bands*

The instability bands of the resonant interactions of the three staircases in figure 2 are shown in the third column of that figure. The bands are too narrow to discern in this plot, with the two borders (that are plotted) merging together. A more detailed picture of instability bands is provided in figure 5, which compares the structure of the bands for staircases with M steps of equal spacing and strength, in the cases of $M = 2$, 4 and 6. The bands are widest for the

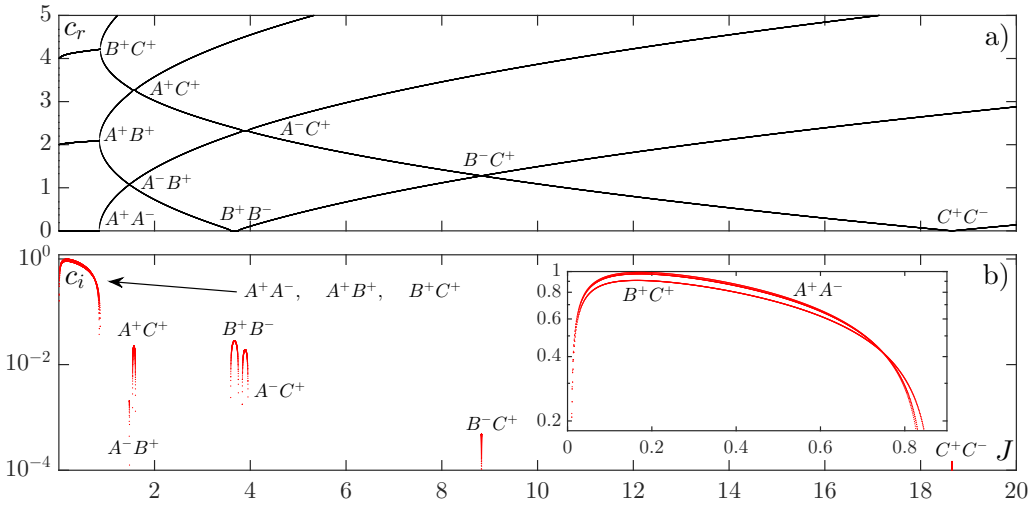

Figure 3. Eigenvalues $c = c_r + i\,c_i$ for a staircase with $M = 6$ steps of equal spacing and strength, plotted against J at $k = 0.01$. (a) shows c_r; the plot is symmetric about $c_r = 0$. (b) plots logarithmically the positive values of c_i. The labels $A^{\pm}$, $B^{\pm}$ and $C^{\pm}$ refer to the interfaces at $y = \pm 1$, ± 3 and ± 5, respectively, and the resonant interactions are identified by pairs of these labels.

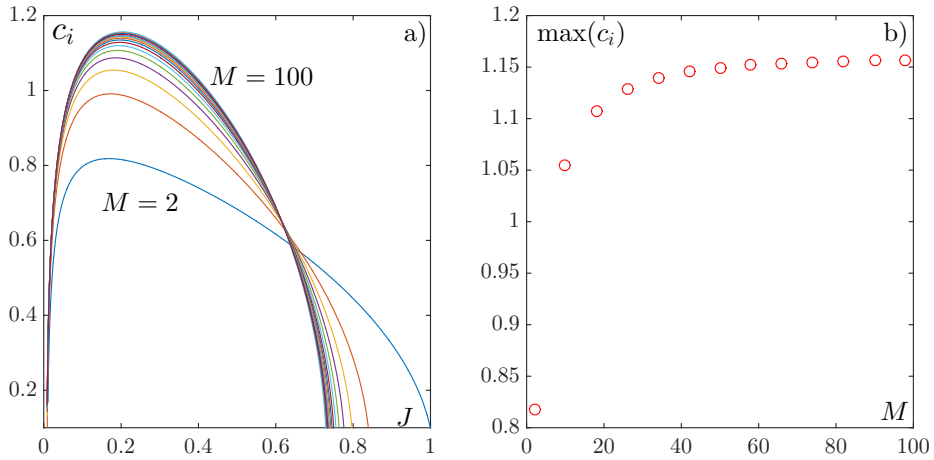

Figure 4. (a) c_i against J for the "core" instability with $c_r = 0$ produced by the interaction of the two interfaces at the centre of staircases with different numbers of steps M, with $k = 0.01$. (b) Max(c_i) as a function of M for the curves in (a).

longest waves and become extremely narrow for $k \gg 1$, where they asymptote to straight lines. The right panel of figure 5 shows the maximum growth rate inside each of the 15 bands for the $M = 6$ staircase, and again illustrates how the interaction is strongest for nearest neighbours but falls off with the distance between the coupled interfacial waves.

The $k \gg 1$ asymptotes of the instability bands can be determined as follows: in the limit of large wave numbers the off-diagonal elements of the matrix in (20) become negligible, reflecting how the vorticity fades quickly away from any interface and thus the waves from different interfaces weakly overlap. This reduces the matrix problem to a product of the

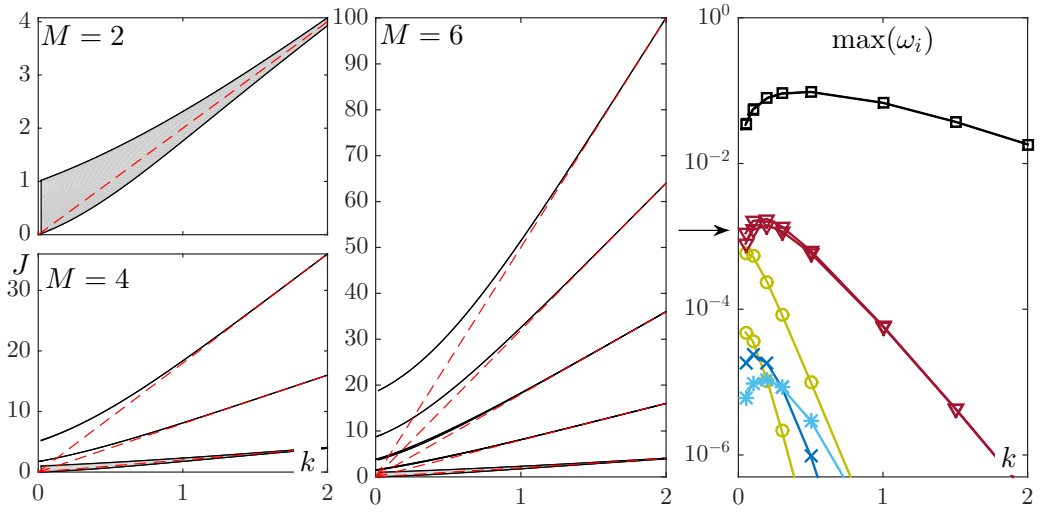

Figure 5. Instability bands (grey with borders plotted as solid lines) for staircase with M =2, 4 and 6 sharp interfaces of equal spacing and strength. The $k \gg 1$ asymptotes are shown by dashed lines. The right-hand panel shows the maximum growth rate $\omega_i \equiv kc_i$ of unstable waves for $M = 6$. Growth rates are labelled as follow: (□) denotes the resonances A^+A^-, $A^\pm B^\pm$ and $B^\pm C^\pm$; (◯) denotes $A^\pm C^\pm$ and $A^\mp B^\pm$; (▽) denotes B^+B^- and $A^\mp C^\pm$; (×) is $B^\mp C^\pm$; (∗) is C^+C^-.

diagonal terms,

$$\prod_{j=1}^{M} \left[2k(y_j - c)^2 - J_j\right] = 0, \tag{23}$$

which implies the modal phase velocities $c = y_j \pm \sqrt{J_j/2k}$, $j = 1, ..., M$. Matching two of the different eigenspeeds furnishes the condition on the respective interfacial Richardson numbers J_j for resonance and therefore the asymptote of an instability band. For equally spaced interfaces of equal strength with M even, $J_j = J$ and $y_j = 2j - M - 1$. Nearest neighbour interfaces then become phase locked for $J = 2k$ and $c = 0, \pm 2, \pm 4, \ldots, \pm(M-2)$. A larger J unlocks the next nearest-neighbour resonances when $J = 8k$ giving $c = \pm 1, \pm 3, \ldots, \pm(M-3)$; third nearest-neighbour resonances are activated when $J = 18k$, where waves drifting at $c = 0, \pm 2, \pm 4, \ldots, \pm(M-4)$ become unstable; and so forth. The repeating structure of the asymptotes of the resonances is thereby elucidated and indicates how to relate the Richardson number to the "order" r of the interaction, defined such that $r = 1$ signifies nearest-neighbour interactions, second nearest-neighbour interactions have $r = 2$, and so on. Evidently, $J = 2r^2k$ for the $k \gg 1$ asymptotes of the instability bands, as observed in figure 5.

For $k \to 0$, (16) has piecewise linear solutions to leading order with

$$-\Psi_{j+1} + \left(2 - \frac{2J_j}{(y_j - c)^2}\right)\Psi_j - \Psi_{j-1} = 0, \quad j = 2, ..., M-1, \tag{24}$$

for $\Psi_j \equiv \psi(y_j)$ and

$$\left(1 - \frac{2J_1}{(y_1 - c)^2}\right)\Psi_1 - \Psi_2 = \left(1 - \frac{2J_M}{(y_M - c)^2}\right)\Psi_M - \Psi_{M-1} = 0. \tag{25}$$

This system has the trivial solutions, $(c, J_j) \to 0$ and $\Psi_1 = \Psi_2 = ... = 1$, corresponding to those captured by the explicit dispersion relation in (19) of the defect theory, which furnishes

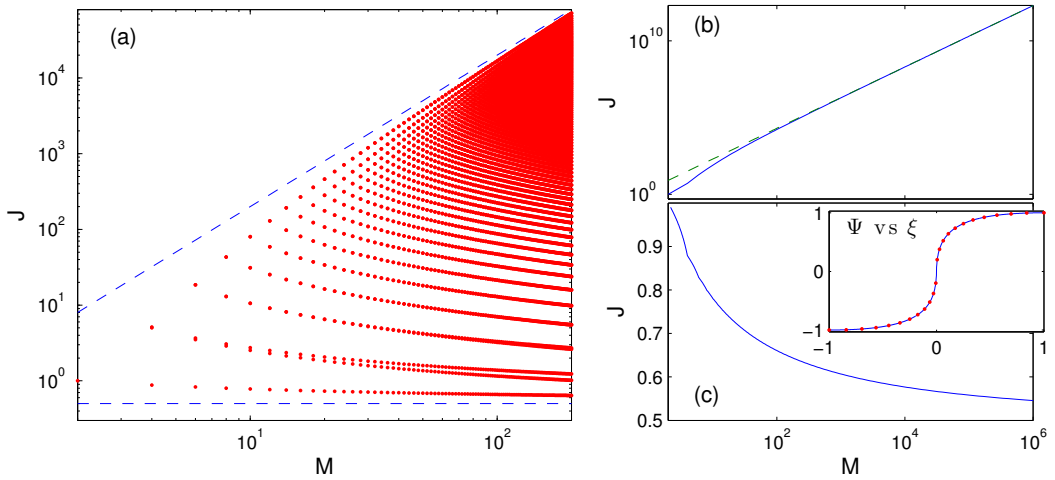

Figure 6. (a) The $k = 0$ intercepts of the $c = 0$ instability bands for uniform staircases with even numbers of steps M. The dashed lines show the bounds $J = \frac{1}{2}$ and $J = 2M^2$. The largest and smallest of these J values are plotted in (b) and (c) over a wider range in M, respectively. The inset in (c) shows the eigenvector Ψ_j plotted against $\xi = (2j - M - 1)/(M - 1)$ for $M = 1000$; the dots show the approximation from taking the continuum limit (see Appendix A).

instead $2 = \sum_{j=1}^{M} (k^{-1} J_j)/(y_j - c)^2$. For the uniform staircase, this implies

$$\frac{2k}{J} \sim \sum_{j=1}^{M} (2j - M - 1 - c)^{-2} \equiv \int_0^\infty x(1 - e^{-Mx}) \frac{\cosh cx}{\sinh x} \mathrm{d}x \qquad (c_r < 1), \tag{26}$$

which predicts that $J \sim 8\pi^{-2} k$ for $c = 0$ and $M \gg 1$. For $J_j = O(1)$, on the other hand, the intercepts of the boundaries of the $c = 0$ instability bands can be computed by iterating (24) and applying the end conditions (25). In particular, for the uniform staircase, the $J-$values of the intercepts can be computed as the eigenvalues of the tridiagonal matrix in (24)-(25), as illustrated in figure 6 for varying M. Evidently, the non-trivial solutions satisfy $\frac{1}{2} < J < 2M^2$ which can be confirmed analytically by working harder with (24); see the Appendix. Note that the highest intercept with $c = 0$ corresponds to the interaction between the steps at the top and bottom of the staircase, and therefore lies above all other instability bands with $c_r \neq 0$. The lowest non-zero eigenvalue, on the other hand, corresponds to the upper edge of the core instability band for $k \to 0$.

Figure 7 shows instability bands for "random" staircases in which $M = 4$ steps have equal strength ($J_j = J$) but are located randomly by setting $y_j = 2j - M - 1 + \delta_j$ with δ_j for $j = 2$ and 3 chosen from a normal distribution with standard deviation $\sigma = 0.2$, and $\delta_1 = \delta_4 = 0$. The left-hand panel of the figure presents a density plot on the $(k, J)-$plane of the number of occurences of the border of an instability band within each of 100×100 bins covering the region $0 \leq k \leq 2$ and $0 \leq J \leq 36$, averaged over 100 different realizations of the staircase. The right-hand panels show similar density plots of c_r and c_i against J for the same realizations at $k = 0.01$. The lines in each panel show the stability boundaries and eigenvalues for a uniform staircase, which thread through the areas with highest density. Thus, again we conclude that the uniformity of a staircase is not essential, and profiles with steps of equal spacing and strength offer a useful guide to the multitude of TCIs in general.

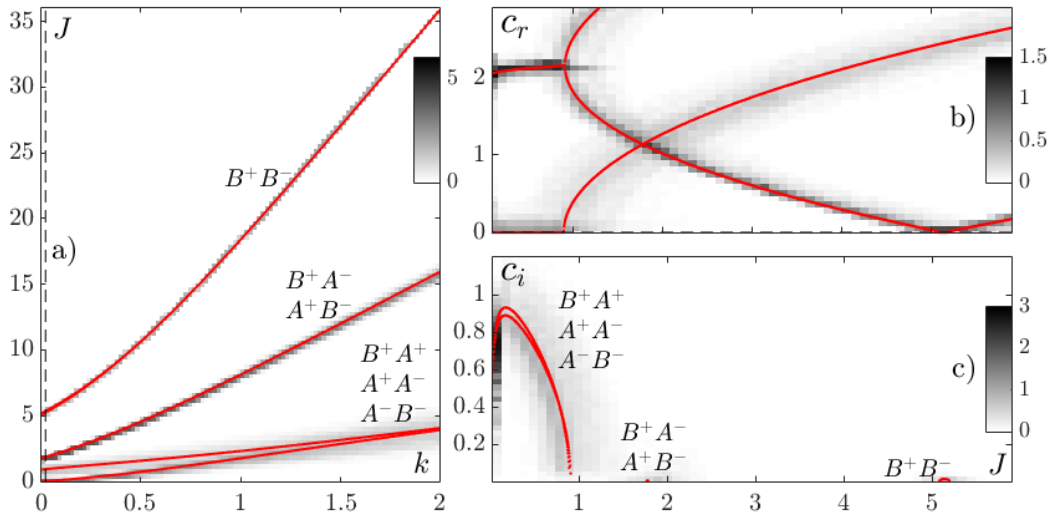

Figure 7. Density maps of the average number of occurrences over 100 realizations of random staircases of (a) stability boundaries and (b)–(c) eigenvalues $c_r + ic_i$ with $k = 0.01$, for 100×100 bins covering the planes shown. The red curves indicate the stability boundaries and eigenvalues for a uniform staircase.

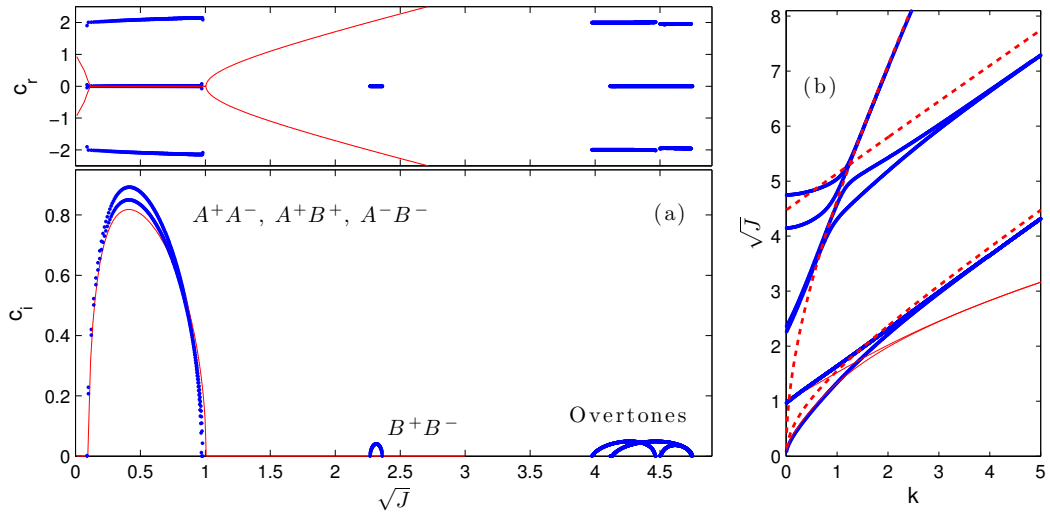

Figure 8. Eigenvalues and stability bands for staircases with $M = 4$ smooth interfaces of thickness $d = 0.2$ (points). The left-hand column (a) shows c_r and c_i against $\sqrt{J}$ for $k = 0.01$ (points). The A^+B^- and A^-B^+ interactions are not detected in these computations. The right-hand column (b) shows the stability bands on the $(k, \sqrt{J})-$plane for the modes with zero phase speed, $c_r = 0$. The dashed lines indicate the estimate in (30) for $(y_j, n) = (1, 0)$, $(3, 0)$ and $(1, 1)$. The (red) curves indicate Taylor's result for two sharp interfaces.

3.2. *Smooth interfaces*

When the interfaces are smoothed over a characteristic thickness d, there are three main changes to the stability results, as illustrated in figure 8. First, when $G > 0$ throughout the fluid depth, the critical-level singularities at $y = c$ rule out neutral waves except along the stability boundaries. Despite this, resonant interactions still occur between disturbances with opposite sign of wave action to generate unstable modes (see figure 8(a)). The resonances lead to bubbles of instability over similar ranges of k and J to the sharp-interface case, at least provided k and J remain order one or less.

Second, when k becomes larger, the modes sample the structure of the interfaces, modifying the asymptotes of the stability bands, such that $J \sim O(k^2)$ (rather than $J \sim O(k)$ as for sharp interfaces; see figure 8(b)). Third, the finite thickness of the interfaces for higher stratifications also leads to the creation of new types of unstable modes. These "overtones" vary sharply and possess nodes within the interfacial regions in a similar fashion to the higher-order Holmboe instabilities described by Alexakis (2005, 2007). As shown in figure 8(a), the overtones have weaker growth rates than the fundamental or primary TCIs. Moreover, the instability bands of the overtones interact with those of the primary modes to enrich the structure of the stability boundaries on the $(k, J)-$plane (figure 8(b)).

The modification to the asymptote of the stability band of the primary modes is seen straightforwardly from (18): for small k and a relatively sharp interface, the integrand is dominated by the localized region around $\xi = y_j$ where $G(y)$ is not small, recovering the earlier estimate of $2k(y_j - c)^2 \sim J_j$. But when k is sufficiently large, the delta-function-like term $ke^{-k|y-\xi|}$ controls the integral, and taking $y = y_j$ leads to a crude alternative estimate, $J_j \sim 4k^2 d(y_j - c)^2$.

A better approximation that also captures the overtone modes follows by arguing that, when $d \ll 1$,

$$\frac{G(y)}{(y-c)^2} \approx \frac{J_j}{2d(y_j - c)^2} \mathrm{sech}^2\left(\frac{y - y_j}{d}\right), \tag{27}$$

in the vicinity of the j^{th} interface, and then solving (16) analytically (by changing variables and recasting the problem as Legendre's equation; *e.g.* Landau and Lifshitz (1977)). The interface supports a localized mode provided

$$J_j = 2d^{-1}(y_j - c)^2(kd + n_j)(kd + n_j + 1), \tag{28}$$

where $n_j = 0$, 1, 2, ... denotes the "order" of the overtone embedded in the interface. The j^{th} and l^{th} interfaces therefore support localized modes simultaneously when

$$c = y_j \pm \sqrt{\frac{dJ_j}{2(kd + n_j)(kd + n_j + 1)}} = y_l \pm \sqrt{\frac{dJ_l}{2(kd + n_l)(kd + n_l + 1)}}, \tag{29}$$

which conveys the richness of the full set of potential resonances. For symmetrically coupled, equal interfaces with $J_j = J_l = J$, $n_j = n_l = n$ and $y_l = -y_j$, the resonant phase speed vanishes and

$$J = \frac{2}{d} y_j^2 (kd + n)(kd + n + 1). \tag{30}$$

The predictions of (30) for $(y_j, n) = (1, 0)$, $(3, 0)$ and $(1, 1)$ are compared with the computed stability boundaries in figure 8.

4. Nonlinear dynamics

We solve the defect equations (14) numerically over the horizontally periodic domain, $0 \leq x \leq 2\pi$ and $-\infty < \eta < \infty$, to examine the fate of multiple TCIs, using the scheme described in more detail in Balmforth *et al.* (2012). Beforehand, however, we review the nonlinear dynamics of a single TCI in the long-wave, weakly stratified and nonlinear limit. Figure 9 displays a numerical solution of a two-interface problem, beginning from the basic state, $\mathscr{Z} = \mathcal{J} \sum_{j=1}^{2} \Theta(\eta - 2j + 3)$, where $\mathcal{J} = 1$ and $\Theta(\eta)$ is the hyperbolic tangent in (11),

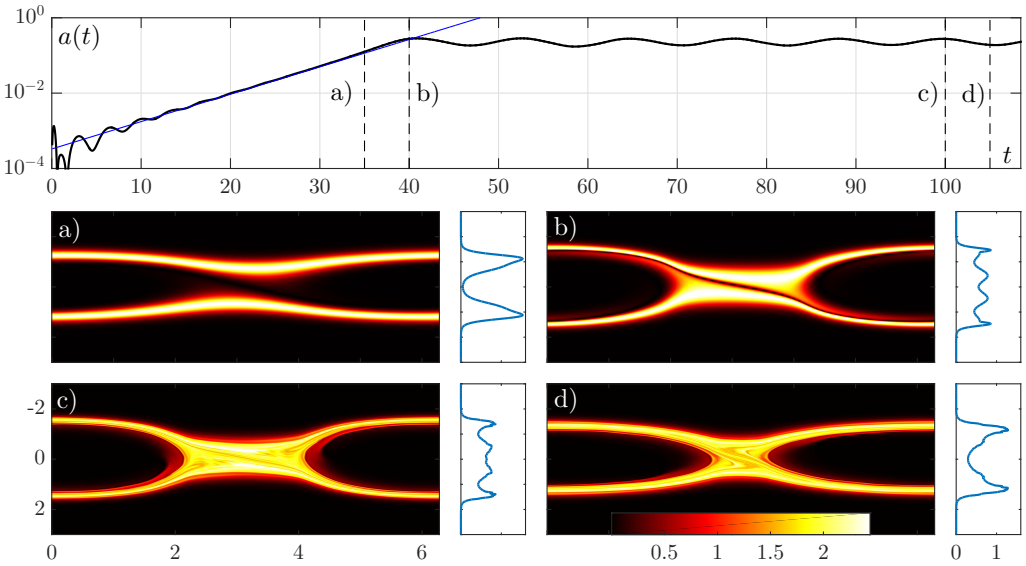

Figure 9. Numerical solution of (14) for two smooth interfaces placed at $\eta = \pm 1$ with characteristic thickness (in η) of 0.2, $J = 1$ and an explicit viscous dissipation term with coefficient $\nu = 10^{-6}$. The top panel shows $a(t) = \sqrt{\sum_{n=1}^{N} |\Phi_n|^2}$, along with the prediction of linear theory. The dashed lines mark the times of the four snapshots of $\mathscr{Z}(x, \eta, \tau)$, plotted as densities over the $(x, \eta)-$plane. On the right of each of these density plots, the horizontal average is plotted.

and we adopt an interface thickness (in η) of $d = 0.2$. The rescaled Richardson number is higher than the critical value $\mathcal{J}_c \approx 0.88$ required for linear instability with $k = 1$, and the unstable mode is triggered by forcing the streamfunction and adding a term $0.01te^{-10t^2}$ to $\Phi_1(t)$ in (13). The snapshots of the $\mathscr{Z}-$field illustrate how the linear mode grows to distort the two interfaces and bring them together, triggering the pinch-off of the intervening layer. A distinctive "Taylor billow" then appears, circulating and pulsating in time. The defect equations are solved including a small viscous term to suppress the generation of unresolved spatial scales; the associated dissipation eventually leads to the decay of the billow.

Figure 10 shows a second computation with four interfaces (and basic state $\mathscr{Z} = \mathcal{J} \sum_{j=1}^{4} \Theta(\eta - 2j + 5)$, with $\mathcal{J} = 1.2$). In this case, there are three unstable modes with phase speeds of $c_r = 0$ and $c_r \approx \pm 2$. All three are triggered by the same forcing of the streamfunction used above, although the core instability is slightly more unstable and becomes visible first, and then grow to pinch off the layers. Three stacked Taylor billows emerge that translate horizontally past each other, with dissipation again smoothing the structure in $\mathscr{Z}$ over long times. Thus, the different TCIs generate co-existing Taylor billows and there is no destructive competition. In the later stages of the computation in figure 10, the central billow is the weaker of the triplet, despite corresponding to the strongest linear instability.

Note how the billows in both of the computations (with two or four interfaces) are bordered by relatively sharp interfaces. Indeed, the horizontally averaged density profile remains step-like: the variable $\mathscr{Z}$ combines the defect vorticity and vertical density gradient, and sharp peaks remain in the horizontal average even after the emergence of the Taylor billow, although they are less pronounced than the peaks of the initial steps. In this sense, the TCIs do not destroy the original staircase. The average structure is not truly representative of a layered mean density profile, however, as the original steps have been strongly distorted and broadened by the TCI. If one were to trace the maxima in density gradient as proxies for interface position, one would observe undulations, mergers and splitting.

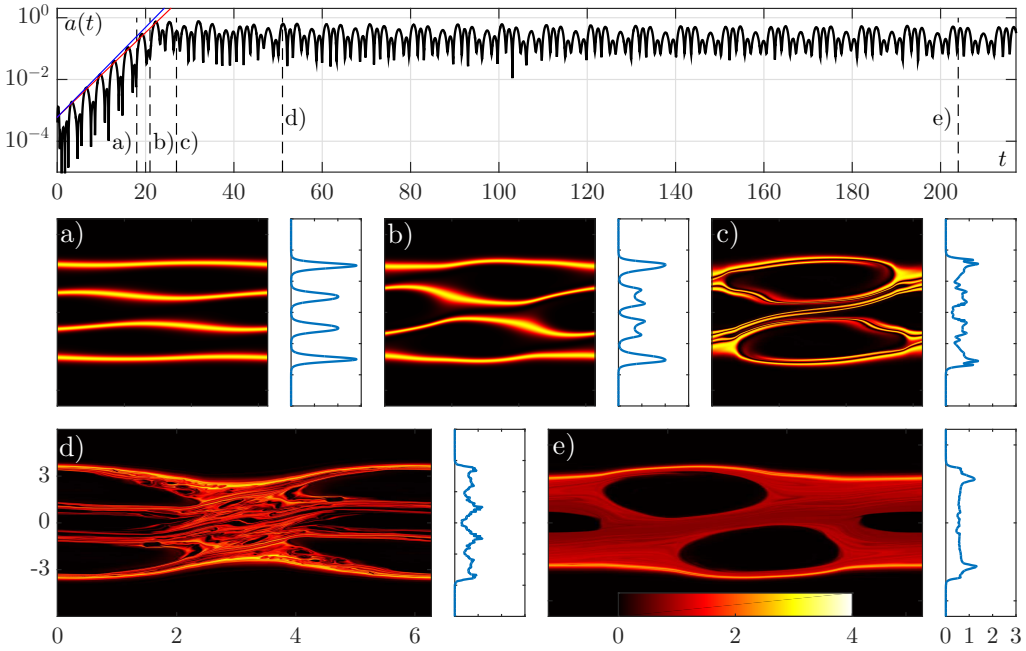

Figure 10. Numerical solution of (14) for four smooth interfaces placed at $\eta = \pm 1$ and ± 3 with characteristic thickness of 0.2, $J = 1.2$ and an explicit viscous dissipation term with coefficient $\nu = 10^{-6}$. The top panel again shows the mode amplitude $a(t)$, along with the linear prediction for the unstable modes (blue for $c_r = 0$ and red for $c_r \approx \pm 2$) and vertical lines indicating the times of the snapshots of $\mathscr{Z}(x, \eta, \tau)$.

Further nonlinear solutions are shown in figure 11, which shows initial-value problems in which the basic four-interface state is perturbed by explicitly adding small amounts of the different unstable modes. At least to begin with, such seeding prompts the pinch off of only one of the layers and its roll up into a single Taylor billow. The billow survives alone for a period, but then nonlinearly excites the unstable modes on the other interfaces. Those modes grow and saturate to generate more billows that co-exist with the parent, furnishing a similar state to that of figure 10.

Co-existence is not a generic feature of Taylor billows that are aligned horizontally, however, as would appear if there were unstable modes with multiple horizontal wavelengths within the domain. In such cases, the billows undergo subharmonic secondary instabilities that lead to mergers and coarsening of the horizontal wavelength. This type of dynamics was catalogued for two interfaces in Balmforth *et al.* (2012), and also occurs when there are more interfaces and vertically stacked billows. Balmforth *et al.* (2012) also demonstrated that TCI is subcritical when two interfaces are sufficiently sharp. This feature again carries over to staircases with multiple TCIs, and implies that billows can be triggered even below the linear instability threshold, either by a sufficiently strong perturbation or by an existing billow occupying a different layer. Details of the computations establishing these results and more can be found in Ponetti (2017).

The continual generation of finer spatial scales in the defect computations leads one to wonder about the fidelity of the long-wave approximation. To address this question we have also performed computations with the full Boussinesq equations (6)–(7) using DIABLO, a parallel Fortran-based numerical code developed by Bewley and Taylor (Taylor 2008). Figure 12 displays such a simulation of TCI for two interfaces. As in the defect computation of figure 9, the linear instability grows to trigger the pinch-off of the intervening layer, which then rolls up

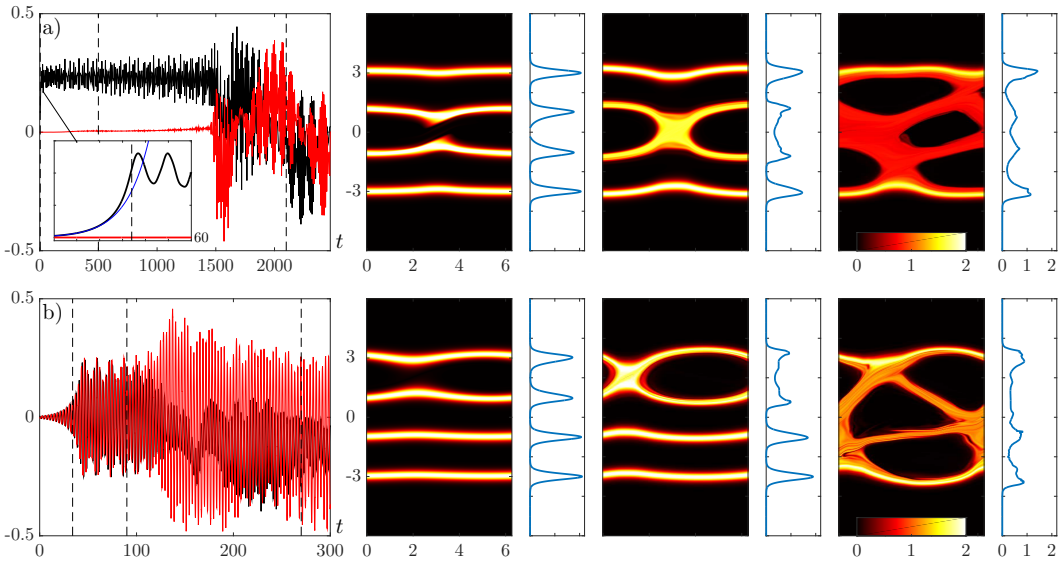

Figure 11. Numerical solutions of the defect problem in which four interfaces are initially perturbed by adding a small amount of the unstable normal mode corresponding to (a) the core instability with $c_r = 0$, and (b) the coupling of the upper two interfaces with $c_r \approx 2$. In each case, the left-hand plot shows a time series of the real (black) and imaginary (red) part of $\Phi_1(t)$, with the vertical dashed lines indicating the times of the snapshots of $\mathscr{Z}$ shown on the right. For (a), the inset shows a magnification of the early times and the prediction of linear theory. Here, $\nu = 10^{-6}$, $J = 0.84$ and $d = 0.2$.

into a billow. Unlike the defect computation, however, in the vicinity of the pinch-off point, the fluid overturns a second time to generate a smaller billow (see also Lee and Caulfield (2001)). This secondary structure endures for a time, but eventually migrates sideways to merge with the main billow, leaving a single structure more like that in the long-time defect solution. The persistence of layers and interfaces in the density field of the saturated billow state is particularly clear in the DIABLO simulation.

Figure 13 shows a second DIABLO simulation, this time with three interfaces. The basic state now has two untable modes, which both grow to create a pair of vertially stacked Taylor billows. As found in the defect computations, the billows are advected by the basic shear and pass non-destructively over one another, persisting until dissipation exacts its toll. We conclude that, for the most part, the defect computations capture the qualitative features of the nonlinear TCI dynamics. The main missing features are secondary structures with an order-one aspect ratio that can appear near the pinch-off point as the main Taylor billows roll up and saturate.

5. Conclusions

Shearing a density staircase by a horizontal mean flow permits the appearance of a multitude of Taylor-Caulfield instabilities (TCIs) driven by the resonant interaction of gravity waves riding on different density interfaces. In this paper, we have provided a linear stability analysis of the situation and presented computations of the nonlinear dynamics that result. The strongest instabilities are those corresponding to wave interactions between neighbouring interfaces. Interactions between more distant interfaces are significantly weaker, as are higher "overtones" that appear when the density profile is smooth, the interfaces have finite thickness and the modes develop nodes within these regions (*cf.* Alexakis (2005, 2007)).

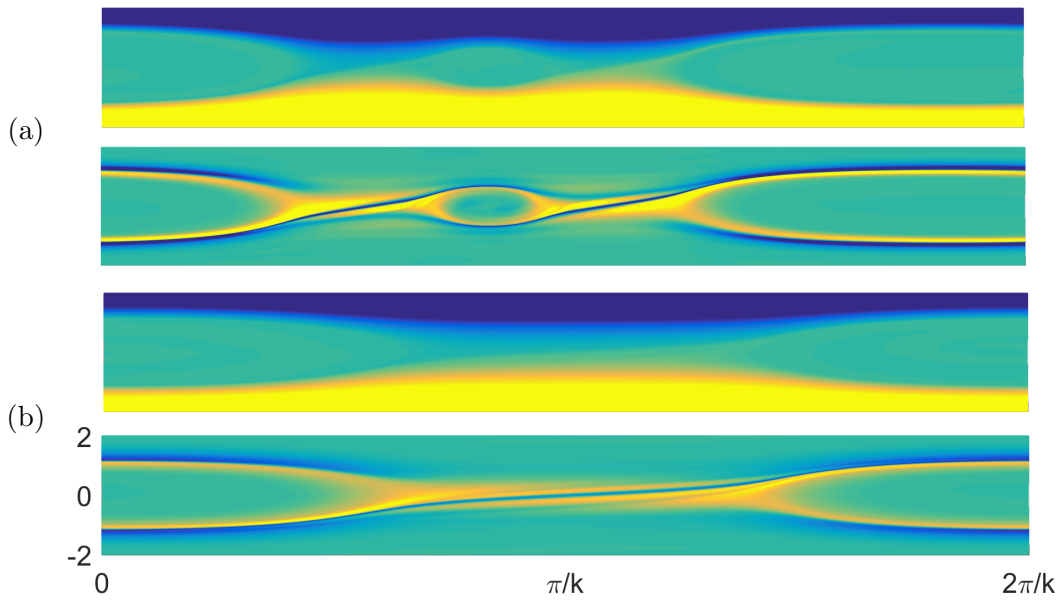

Figure 12. Numerical solutions of the full problem with two interfaces kicked with a low-amplitude perturbation. Shown are density plots of total buoyancy $B(y)+b(x,y,t)$ and vorticity $\zeta(x,y,t)$ over the $(x,y)-$plane for (a) a time just after the initial saturation of the instability and (b) 320 time units later. Computations are performed including viscous and density diffusion, with parameters both equal, $\nu=\kappa=4.44\times10^{-5}$. The horizontal domain length is $2\pi/k\equiv10\pi$.

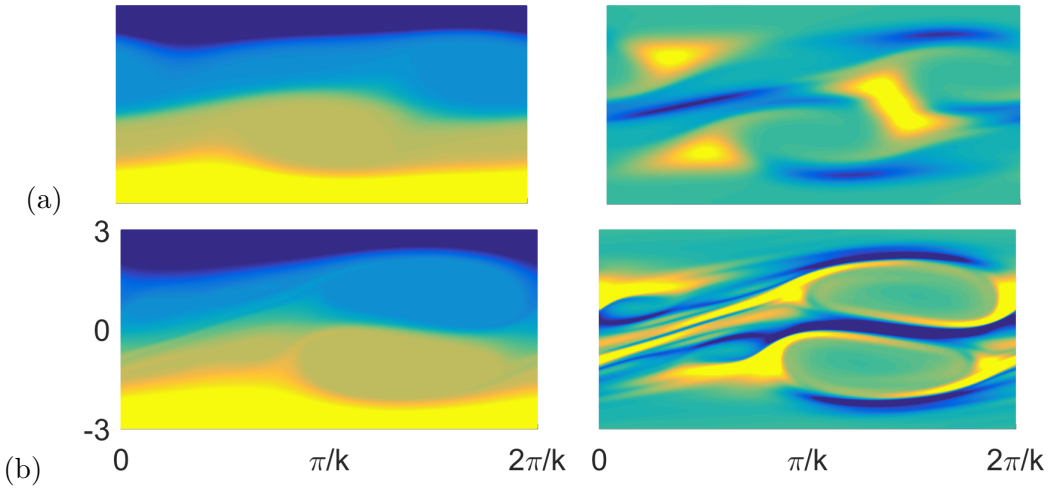

Figure 13. Numerical solutions of the full problem with three interfaces kicked with a low-amplitude perturbation. Shown are density plots of total buoyancy $B(y)+b(x,y,t)$ and vorticity $\zeta(x,y,t)$ over the $(x,y)-$plane for (a) a time just after the initial saturation of the instability and (b) 72 time units later. The viscous parameter is $\nu=2.67\times10^{-4}$ and density diffusion parameter is $\kappa=8.89\times10^{-5}$. The horizontal domain length is $2\pi/k\equiv4\pi$.

The nonlinear numerical computations indicate that the nearest-neighbour TCIs roll up the intervening layer, to create distinctive Taylor billows. With multiple steps in the staircase, the nearest neighbour resonances drive a vertically stacked array of Taylor billows. These structures pass by and disturb one another as they are carried along by the underlying shear, but do not destructively interfere. This is unlike the dynamics of horizontally arrayed Taylor billows, that destructively merge together much like Kelvin-Helmholtz vortex pairing.

Although the basic state is significantly re-arranged by the Taylor billows, sharp interfaces survive but become somewhat broadened and distorted, and a layer-like structure remains in

horizontal averages. Thus, in this sense and despite saturating at finite amplitude, TCI does not destroy the density staircase. However, tracking the vertical positions of the interfaces in the horizontal would reveal significant migration as well as fusion and fission.

We close by noting that our nonlinear computations are mostly conducted exploiting a long-wave, weakly stratified approximation (the stratified defect theory of Balmforth *et al.* (2012)). Such computations potentially miss a host of secondary instablities related to finite-wavelength and diffusive effects, which can destroy the Taylor billows themselves. Whether density layering survives in such a situation remains to be seen.

References

Alexakis, A., On Holmboe's instability for smooth shear and density profiles. *Physics of Fluids*, 2005, **17**, 084103.

Alexakis, A., Marginally unstable Holmboe modes. *Physics of Fluids*, 2007, **19**, 054105.

Baines, P. and Mitsudera, H., On the mechanism of shear flow instabilities. *J. Fluid Mech.*, 1994, **276**, 327–342.

Balmforth, N.J., Roy, A. and Caulfield, C.P., Dynamics of vorticity defects in stratified shear flow. *J. Fluid Mech.*, 2012, **694**, 292–331.

Balmforth, N., Llewellyn Smith, S. and Young, W., Dynamics of interfaces and layers in a stratified turbulent fluid. *J. Fluid. Mech.*, 1998, **355**, 329–358.

Cairns, R., The role of negative energy waves in some instabilities of parallel flows. *J. Fluid Mech.*, 1979, **92**, 1–14.

Carpenter, J., Balmforth, N. and Lawrence, G., Identifying unstable modes in stratified shear layers. *Physics of Fluids*, 2010, **22**, 054104.

Carpenter, J., Tedford, E., Heifetz, E. and Lawrence, G., Instability in stratified shear flow: Review of a physical interpretation based on interacting waves. *Applied Mechanics Reviews*, 2011, **64**, 060801.

Carpenter, J. and Timmermans, M., Temperature steps in salty seas. *Physics Today*, 2012, **65**, 66–67.

Caulfield, C. P., Multiple linear instability of layered stratified shear flow. *J. Fluid Mech.*, 1994, **258**, 255–285.

Drazin, P.G. and Reid, W.H., *Hydrodynamic stability*, 2004 (Cambridge university press).

Eaves, T. and Caulfield, C. P., Multiple instability of layered stratified plane Couette flow. *J. Fluid Mech.*, 2017, **813**, 250–278.

Landau, L. and Lifshitz, E., *Quantum Mechanics: Non-Relativistic Theory*, Vol. 3, 1977 (Pergamon).

Lee, V. and Caulfield, C. P., Nonlinear evolution of a layered stratified shear flow. *Dynamics of atmospheres and oceans*, 2001, **34**, 103–124.

Oglethorpe, R., Caulfield, C. P. and Woods, A.W., Spontaneous layering in stratified turbulent Taylor–Couette flow. *J. Fluid Mech.*, 2013, **721**, R3.

Park, Y., Whitehead, J. and Gnanadesikan, A., Turbulent mixing in stratified fluids: layer formation and energetics. *J. Fluid. Mech.*, 1994, **279**, 279–311.

Ponetti, G., The title. Ph.D. Thesis, University of Palermo, 2017.

Radko, T., Mechanics of merging events for a series of layers in a stratified turbulent fluid. *J. Fluid Mech.*, 2007, **577**, 251–273.

Schmitt, R., Double diffusion in oceanography. *Annu. Rev. Fluid Mech.*, 1994, **26**, 255–285.

Sutherland, B., *Internal gravity waves*, 2010 (Cambridge University Press).

Taylor, G., Effect of variation in density on the stability of superposed streams of fluid. *Proc. R. Soc. London*, 1931, **132**, 499–523.

Taylor, J., *Numerical simulations of the stratified oceanic bottom boundary layer*, 2008 (ProQuest).

Turner, J., Multicomponent convection. *Annu. Rev. Fluid Mech.*, 1985, **17**, 11–44.

Appendix A:

For uniform staircases with $J_j = J$ and $y_j = 2j - N - 1$, the introduction of the variable $r_j = \Psi_{j+1}/\Psi_j$, recasts the tridiagonal system (24) into the form,

$$r_j = 2 - \frac{2J}{y_j^2} - \frac{1}{r_{j-1}}, \tag{A.1}$$

which can be iterated from $j = \frac{1}{2}M$ up to M using the starting condition $r_{M/2} = \pm 1$, corresponding to solutions for Ψ_j that are even or odd, respectively. The termination condition in (25) translates to $r_{M-1} = [1 - 2J/(M-1)^2]^{-1}$, and determines the $J-$value of the $k = 0$ intercept of an instability band.

If $J > 2M^2$, $2 - 2Jy_j^{-2} < -2$ and it then follows that $r_j < -1$ for $0 < j < M - 1$. It is not therefore possible to satisfy the termination condition $r_{M-1} = [1 - 2J/(M-1)^2]^{-1} > -\frac{1}{3}$ if $M \gg 1$. Thus, $J \leq 2M^2$. Moreover, when J is just less than $\frac{1}{2}M^2$, we may alternatively iterate $r_{j-1} = (2 - 2Jy_j^{-2} - r_j)$ from $j = \frac{1}{2}M$ back to $j = 1$ and impose the end condition $r_1 = 1 - 2J/(M-1)^2$. If $J \gg 1$, the first iterations give $y_j \sim -\frac{1}{2}y_j^2(J - y_j^2)^{-1}$. Eventually, however, one reaches an iterate $j \sim \frac{1}{4}M^2$ with $J < 2y_j^2$, beyond which r_j converges instead towards unity for $r \geq 2$. But with $r_2 \to 1$, the termination condition is met immediately. Thus, there are solutions with J arbitrarily close to $\frac{1}{2}M^2$ for $M \gg 1$.

For the smallest non-zero solution for J, iteration of (A.1) furnishes the limiting solution,

$$r_j \sim 1 + (2j - M - 1)^{-1}[1 + \sqrt{1 - 2J}], \quad 2j - M - 1 \gg 1, \tag{A.2}$$

provided $J < \frac{1}{2}$. The termination condition reduces to $r_{M-1} = 1$ if $J = O(1)$ and M is sufficiently large that $2J/y_M^2 \to 0$, which indicates that there are therefore no solutions with $0 < J < \frac{1}{2}$. When $J > \frac{1}{2}$, the solution iterates away from $r_j = 1$ and converges to a different solution that can be approximated by taking the continuum limit of (24):

$$\xi^2 \frac{\mathrm{d}^2\Psi}{\mathrm{d}\xi^2} + \tfrac{1}{2}J\Psi = 0, \quad \xi \equiv \frac{2j - M - 1}{M - 1}. \tag{A.3}$$

Thence, for $\xi > 0$,

$$\Psi \sim \sqrt{\xi}\sin\left(\tfrac{1}{2}\sqrt{2J-1}\log\xi - \tan^{-1}\sqrt{2J-1}\right), \tag{A.4}$$

such that $\Psi'(1) = 0$, which corresponds to the continuum limit of (25). The solution (A.4) can be extended to $\xi < 0$ as either an even or odd function, and the match of $\Psi(\xi + \Delta)/\Psi \approx 1 + \Delta\Psi'(\xi)/\Psi(\xi)$ to the iterative solution r_j for $1 \gg (2j - M - 1) \gg M$ thereby dictates J, where $\Delta = 2/(M-1) \ll \xi = (2j - M - 1)/(M - 1) \ll 1$. The inset in figure 6(c) compares the approximation of $\Psi(\xi)$ to the numerically computed eigenvector of the tridiagonal matrix corresponding to the smallest non-zero eigenvalue, using that value of J in (A.4). At this stage, one can observe that the lowest solution for J converges to $\frac{1}{2}$ as $M \to \infty$: $\Psi(\xi + \Delta)/\Psi \sim 1 + J\Delta/\xi \equiv 1 + 2J/(2j - M - 1)$, in line with the limit of (A.2), if $J \to \frac{1}{2}$.